nature energy

Article

https://doi.org/10.1038/s41560-026-02068-9

Close-space sublimation as a versatile deposition process for efficient perovskite silicon tandem solar cells

Received: 14 August 2025

Accepted: 20 April 2026

Published online: 19 May 2026

Check for updates

Alexander Diercks[1,6], Sofía Chozas-Barrientos[2,6], Lidón Gil-Escrig[2], Federico Ventosinos[2,3], Inma Gomar-Fernández[2], Cristina Roldán-Carmona[2], Nathan Rodkey[2], Tonghan Zhao[4], Julian Petermann[1,4], Maximiliano Senno[2], Vladimir Held[2], Perrine Carroy[5], Delfina Muñoz[5], Paul Fassl[1,4], Michele Sessolo[2], Ulrich W. Paetzold[1,4,7] ✉ & Henk J. Bolink[2,7] ✉

The envisaged breakthrough of perovskite photovoltaic technologies demands rapid advances in scalable and robust high-throughput fabrication methods. Here we present close-space sublimation (CSS) as a vacuum-based, industrially relevant deposition method for the conversion of sublimed PbI_2 inorganic scaffolds into high-quality wide-bandgap perovskite absorbers ($MAPb(I_{0.79}Br_{0.21})_3$, 1.64 eV), employing a reusable mixed-halide organic source for stable bandgap control. We provide mechanistic insights into the substitution-reaction-limited CSS process and achieve power conversion efficiencies (PCEs) of up to 18.5% for fully vacuum-processed p–i–n single-junction devices. Monolithic integration in tandem solar cells onto planar, nano- and micro-textured silicon bottom cells reveals consistent optoelectronic and morphological properties across all configurations without requiring adjustments of deposition parameters, as corroborated by comprehensive characterization techniques. The resulting perovskite/silicon tandem solar cells reach PCEs up to 24.3%, with minimal variation across the different bottom cells. Our findings highlight the broad process window and versatility of CSS, positioning it as an industry-suitable deposition method for solvent-free high-throughput fabrication.

Bridging the gap between laboratory- and industrial-scale fabrication remains a key challenge for advancing industrialization of perovskite photovoltaics[1–4]. In this regard, advances on industrially relevant deposition methods for rapid processing and efficient upscaling are pivotal[1,5–7]. This urge has been further amplified by recent reports of power conversion efficiencies (PCEs) exceeding 34% in perovskite/silicon tandem solar cells (TSCs), surpassing those of market-leading silicon technologies[8]. Despite being severely underrepresented in literature, vapour-phase deposition offers key benefits when it comes to scalable processing, that is, homogeneous large-area coating and continuous in-line processing[2,9–12]. Furthermore, vapour-phase deposition allows for conformal coverage of textured surfaces, essential for the monolithic integration of perovskite absorbers into two-terminal (2T) tandem solar cells with textured silicon bottom cells[5,13,14]. To date, most studies exploring vapour-phase deposition for the fabrication of perovskite solar cells (PSCs) have focused on either co-deposition

[1]Light Technology Institute, Karlsruhe Institute of Technology, Karlsruhe, Germany. [2]Instituto de Ciencia Molecular, Universidad de Valencia, Paterna, Spain. [3]Instituto de Física del Litoral (IFIS-Litoral), CONICET-UNL, Santa Fe, Argentina. [4]Institute of Microstructure Technology, Karlsruhe Institute of Technology, Eggenstein-Leopoldshafen, Germany. [5]Université Grenoble Alpes, CEA, LITEN, Campus INES, Le Bourget-du-Lac, France. [6]These authors contributed equally: Alexander Diercks, Sofía Chozas-Barrientos. [7]These authors jointly supervised this work: Ulrich W. Paetzold, Henk J. Bolink. ✉e-mail: ulrich.paetzold@kit.edu; henk.bolink@uv.es

or sequential layer deposition from point sources in high vacuum. Reported PCEs using these approaches have reached up to 23.1% and 26.4% in single-junction (SJ) PSC configurations, respectively[15,16]. The highest reported PCE for a fully textured 2T perovskite/silicon TSC fabricated via vapour-phase deposition is 24.5% using a co-deposited $MA_{0.5}FA_{0.63}PbI_{3.13}$ perovskite top cell as demonstrated by Roß et al. (MA = methylammonium, FA = formamidinium)[13]. Whereas these results highlight the potential of vapour-phase deposition processes for the fabrication of high-efficiency perovskite-based solar cells, their slow deposition rates compared to solution-based methods remain an important hurdle to efficient industrialization[17,18]. For conventional thermal co-evaporation, effective perovskite deposition rates are typically in the few nanometres per minute range, particularly for FA-based compositions. As discussed in our recent work by Petry et al., while inorganic precursors can in principle be deposited at sufficiently high rates using industrially relevant linear sublimation sources, the limited thermal stability of FAI fundamentally constrains the maximum attainable organic deposition rate, making high-throughput deposition challenging[19].

Close-space sublimation (CSS) has recently emerged as a new high-rate deposition technique for perovskite photovoltaics that bears the potential to reach high deposition rates for the organic precursor components, while maintaining both high performance and the key advantages of vapour-phase deposition[20,21]. In CSS, the gap between the substrate with the inorganic scaffold and the organic precursor source is drastically reduced compared to established thermal evaporation set-ups. Thereby, for gaps of a few millimetres or less, the organic precursors can be deposited at much higher rates and elevated working pressures, typically in the range of 1–100 mbar (refs. 20,21). Moreover, material usage is much more efficient compared to sublimation from point sources. In cadmium telluride (CdTe) thin-film photovoltaics, CSS has been extensively developed as a scalable deposition technique[22]. Although modern CdTe manufacturing lines employ vapour transport deposition, both approaches rely on the same fundamental principle of high-flux sublimation and short-distance vapour transport at elevated pressures, demonstrating their industrial compatibility for high-throughput large-area thin-film manufacturing. Notably, CSS processes employ elevated substrate temperatures during the deposition, resulting in an in situ conversion of the inorganic scaffold to the perovskite phase[21]. First reports on a CSS-based fabrication process for $MAPbI_3$ PSCs were published in 2015 by Li et al. achieving PCEs of up to 16.2% (ref. 23). Efficiencies have since improved, exceeding 22% in a low-bandgap, Br-free PSC in the n–i–p architecture, which currently represents the highest-performing configuration for SJ devices[24]. Guesnay et al. reported in 2024 the first wide-bandgap (WBG) PSC, reaching maximum PCEs of 16.8% for a bandgap of 1.63 eV (ref. 25). Further studies on similar fabrication processes, mainly close-space vapour transport, show PCEs of up to 22.45% for narrow-bandgap perovskite compositions[26–29] and up to ~20% in SJ solar cells with widened bandgap[30–32]. Zhang et al. reported on perovskite/silicon TSCs with PCEs of up to 26.9%, which however rely on untextured planar silicon bottom cells, non-ideal top-cell bandgap and a Br-free organic CSS precursor, limiting its industrial relevance[31]. Recently, Kuba et al. demonstrated perovskite/silicon TSCs with PCEs exceeding 29% on float-zone silicon wafers using a FA-based CSS process with tunable bandgap[30]. Critically, these previous studies do not demonstrate stable and reusable source designs as required for industrial fabrication processes because they implement organic thin-film sources prepared by solution processing onto a glass substrate or Si wafer[25–32]. In that regard, Rodkey et al. demonstrated a fully solvent-free CSS set-up employing a reusable organic source design, operational for more than 28 depositions, reaching maximum PCEs of 18.7% for $FACsPbI_3$:Cl PSCs[21]. In a following study, Gomar–Fernández et al. implemented a large-area CSS organic source (96 cm^2) to fabricate $MAPbI_3$ PSCs in the p–i–n architecture reaching PCEs of up to 18.8% (ref. 33). Despite this recent progress, WBG perovskites suitable for tandem photovoltaics are still elusive and have yet to be demonstrated using industrially compatible CSS processes.

In this work, we reveal that it is not trivial to prepare mixed-halide WBG perovskites using CSS, yet demonstrate a mitigating strategy that allows for their reproducible preparation at high deposition rates. We establish that bromide incorporation into the perovskite film can only be obtained by employing a mixed-halide organic source, where the ratio of the used halide salts governs the bandgap of the final perovskite absorber layer. These CSS-processed WBG perovskites are used to fabricate efficient SJ PSCs with champion PCEs of 18.5% and 16.2% in opaque and semitransparent device architectures, respectively. Furthermore, we successfully integrate these high-quality WBG perovskite absorbers into 2T perovskite/silicon TSCs, reaching PCEs of 23.5% on planar and 24.3% on textured silicon bottom cells. In-depth characterization of the CSS-processed perovskite absorbers deposited on the differently textured silicon bottom cells reveals consistent morphological and optoelectronic properties, underscoring the broad process window of the optimized CSS process. Our results demonstrate the high versatility of CSS for the fabrication of efficient SJ PSCs and 2T perovskite/silicon TSCs, proving its potential as an industrial-scale high-throughput fabrication process.

Close-space sublimation process

In this work, a sequential vapour-phase deposition process is pioneered to fabricate MA-based WBG perovskite absorber layers for application in 2T perovskite/silicon TSCs (Fig. 1a). The first step comprises the thermal sublimation of the inorganic precursors leading to a 250-nm-thick inorganic scaffold layer. The second step involves the close-space sublimation of the organic cations. Because during the CSS step the substrates are maintained at a temperature close to that of the source, the sublimed organic component reacts in situ with the inorganic scaffold and starts forming the polycrystalline perovskite thin film[21]. The close gap between the substrate and the organic source allows the CSS deposition to be easily controlled by the pressure in the vacuum chamber. Deposition of the organic precursor starts as soon as the chamber pressure reaches the 1 mbar range. At this pressure the mean free path of the material sublimed from the continuously heated organic source is comparable to sub-millimetre scales between source and substrate. The deposition is terminated by venting the chamber with N_2 and returning it to atmospheric pressure.

Fabrication of WBG perovskites via sequential sublimation is commonly done by subsequently depositing a mixed-halide inorganic scaffold and an alkylammonium iodide A-cation[34]. A few research groups have recently advanced this process, achieving high-performance SJ PSCs using perovskite absorbers over a wide range of bandgaps[35–37]. Following this strategy, we attempt to fabricate WBG perovskite absorbers via CSS, by using a pure methylammonium iodide (MAI) organic source to convert the mixed-halide inorganic scaffold. Different $Pb(I:Br)_2$ ratios (PbI_2, $Pb(I_{0.67}Br_{0.33})_2$, $Pb(I_{0.33}Br_{0.67})_2$, $PbBr_2$) are used to investigate the impact of bromine content on the bandgap of the final perovskite. For the different $Pb(I:Br)_2$ ratios, both precursors are mixed in the corresponding molar ratios and melted at 360 °C in N_2 at atmospheric pressures before sublimation[38,39].

To elucidate the stepwise reaction mechanism during CSS, we conducted an ex situ time-resolved conversion study using cross-sectional scanning electron microscopy (SEM) to probe the intermediate states of the PbI_2-to-perovskite transformation (Supplementary Fig. 1). For this purpose, the growth process was interrupted after different times of the CSS process step. The data reveal a clear top-down conversion pathway where a thin perovskite layer forms at the surface within the first minute and subsequently propagates deeper into the PbI_2 scaffold with increasing conversion time. This depth-dependent evolution is

https://doi.org/10.1038/s41560-026-02068-9

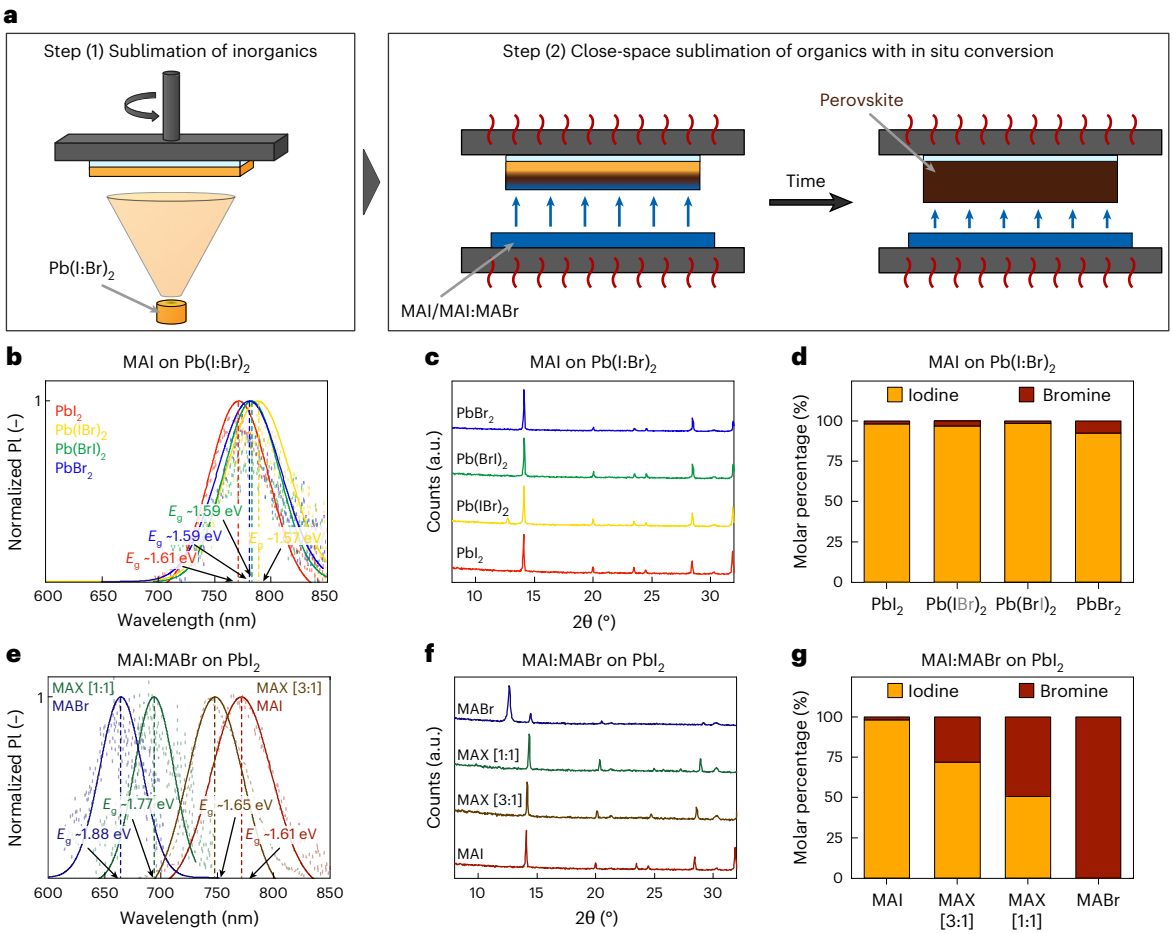

Fig. 1 | Compositional engineering of wide-bandgap perovskites via close-space sublimation. a, Schematic of the two-step processed perovskite absorber layer using physical vapour deposition from a point source for the inorganic precursor materials ($Pb(I:Br)_2$) and close-space sublimation from a large-area source for the organic precursor materials (MAI:MABr) with in situ conversion to the perovskite phase. **b**, Photoluminescence (PL) analysis of perovskite films after conversion of different inorganic scaffolds (PbI_2, $Pb(I_{0.67}Br_{0.33})_2$, $Pb(I_{0.33}Br_{0.67})_2$, $PbBr_2$) with a pure MAI organic source and a process time of 35 min, respectively. **c**, X-ray diffraction (XRD) pattern of the corresponding perovskite thin films. **d**, Corresponding iodine-to-bromine ratios from electron dispersive X-ray (EDX) measurements of the fabricated perovskite thin films. **e**, PL analysis of perovskite films after conversion of a pure PbI_2 inorganic scaffold with different organic source compositions of MAI:MABr (1:0, 3:1, 1:1, 0:1). **f**,**g**, XRD pattern and iodine-bromine-ratios from EDX analyses of the corresponding perovskite thin films, respectively.

corroborated by grazing-incidence XRD, which shows early formation of a perovskite-rich surface layer while PbI_2 persists beneath. The gradual disappearance of the PbI_2 diffraction signal and the concurrent increase in optical absorbance further confirm a progressive, diffusion-limited incorporation of the organic species rather than a homogeneous bulk conversion. Together, these results provide direct morphological and structural evidence that CSS proceeds through a sequential, surface-initiated recrystallization process in which the organic vapour progressively converts the underlying PbI_2 scaffold.

Surprisingly, after full conversion, all perovskite films exhibit a bandgap similar to that of pure $MAPbI_3$, extracted from photoluminescence (PL) measurements (Fig. 1b and Supplementary Fig. 2), implying that bromine is removed from the film during the CSS conversion step. XRD analyses of the corresponding perovskite films confirm the formation of $MAPbI_3$, irrespective of the bromine content of the inorganic scaffold (Fig. 1c). Remarkably, even perovskite films fabricated with a pure $PbBr_2$ inorganic scaffold present a nearly bromine-free composition (Fig. 1d). Hence, we show, in agreement with previous reports, that the MAI deposition via CSS leads to a halide exchange reaction of iodine and bromine during the in situ conversion[32]. Taken together, these findings show that the halide composition during CSS is governed primarily by the vapour-phase halide flux rather than by the initial inorganic scaffold. They further clarify the halide exchange mechanism through which bromide is displaced and can leave the film under MAI-rich conditions, providing a coherent explanation for the progressive loss of Br during MAI-driven conversion and supporting the expectation that the displaced Br exits the film in the form of volatile MABr. These findings demonstrate that mixed-halide perovskites cannot be fabricated by adjusting the halide ratio through the inorganic scaffold.

To overcome this limitation, we adopt a revised strategy in which bromine is incorporated exclusively via the organic source. For this, a pure PbI_2 inorganic scaffold is converted using mixed MAI:MABr organic sources with different relative weight ratios (1:0, 3:1, 1:1 and 0:1) to systematically study the influence on the bandgap of the final perovskite. PL measurements reveal a blue shift in the PL peaks of the perovskite absorbers as the bromide content in the organic source increases. Remarkably, when using a pure MABr organic source, the perovskite exhibits a bandgap of 1.88 eV (Fig. 1e), suggesting the formation of a Br-rich mixed-halide perovskite composition, as confirmed by the corresponding XRD pattern (Fig. 1f). Furthermore, EDX analyses of all perovskite films show that an increasing bromide content in the mixed organic source leads to a corresponding rise in bromide content in the final perovskite film (Fig. 1g), revealing a reversed halide exchange reaction.

https://doi.org/10.1038/s41560-026-02068-9

Table 1 | Photovoltaic parameters of the best-performing PSCs for the different architectures. Values in bold represent the champion device and the corresponding photovoltaic parameters

	PCE (%)	FF (%)	J_{sc} (mA cm^{-2})	V_{oc} (V)
as deposited	14.6	70.2	19.6	1.06
annealed	16.2	74.5	19.7	1.10
with $EDAI_2$	17.4	79.9	19.1	1.14
with $EDAI_2$ and LiF	**18.5**	**79.2**	**20.3**	**1.15**
ST top illuminated	16.2	75.3	19.5	1.10

These findings shed light on the conversion mechanism during the CSS process. Varying the halide ratio in the inorganic precursor is consistent with halide exchange reactions occurring during the CSS process[40,41]. The composition of CSS-processed perovskite absorbers is governed primarily by the organic source, where the MAI:MABr ratio in the vapour phase dictates the final halide content of the resulting perovskite absorber. Importantly, this vapour-dominated halide exchange does not appear to perturb the composition of the organic source itself (Supplementary Table 1). EDX measurements of the MAI:MABr powder before use and after a cumulative 540 min of CSS operation show that the Br:I ratio remains essentially unchanged, which is corroborated by the similar sublimation enthalpies found for MABr and MAI[42,43]. Hence, this indicates that the mixed-halide organic source acts as a stable halide reservoir during repeated CSS processes and that the dynamic halide exchange observed in the growing perovskite film is confined to the film environment and does not deplete or alter the source. Consequently, the steady vapour composition provides a robust and reliable halide flux whose composition is governed by the ratio of organic components in the reusable source and that consistently governs the final perovskite stoichiometry. In summary, the dynamic exchange process explains why Br originating from the inorganic scaffold is largely removed, whereas Br supplied through the organic vapour is efficiently incorporated. The final perovskite stoichiometry reflects the halide ratio in the vapour phase during the CSS process rather than the initial scaffold composition.

Efficient wide-bandgap perovskite solar cells

Having demonstrated the ability to tune the bandgap of the perovskite absorber via the composition of the organic source, SJ PSCs are fabricated using a mixed MAI:MABr organic source with a relative mass ratio of 3:1, which results in a bandgap of 1.64 eV, as is confirmed by the external quantum efficiency (EQE) analysis of the resulting devices (Fig. 1d). Within only 10 min at 1 mBar the inorganic scaffold is fully converted into the final methylammonium lead iodide:bromide perovskite film with a ($MAPb(I_{0.79}Br_{0.21})_3$) composition as determined from EDX measurements (Supplementary Fig. 3). Subsequent to the CSS step, an additional annealing step of the fabricated perovskite absorber layer is found to further improve the performance of the final PSCs.

Whereas as-deposited PSCs already exhibit respectable performance with median PCEs of 14.4% (Supplementary Figs. 4 and 5 and Table 1), additional annealing of 10 min at 100 °C in a humidity-controlled environment (relative humidity ~35%) boosts these PCEs up to more than 16% (Supplementary Fig. 4 and Table 1). Ultimately, implementing an optimized fully vacuum-processed layer stack (LiF/indium tin oxide (ITO)/p-doped TaTm/TaTm/$MAPb(I_{0.79}Br_{0.21})_3$/$EDAI_2$/$C_{60}$/BCP/Ag) (Fig. 2a), brings the median efficiency up to 18.1% with the champion device achieving a maximum PCE of 18.5%, with negligible hysteresis and a stabilized power output of 18.2% under maximum power point tracking (Fig. 2c). The current–voltage (*J*–*V*) curves recorded at different scan rates are nearly identical, confirming hysteresis-free device operation (Supplementary Fig. 6 and Supplementary Table 2). The 50 mV increase in open-circuit voltage (V_{OC}) and 0.7 mA cm^{-2} enhancement in short-circuit current density (J_{SC}) compared to the annealed device are attributed to the use of $EDAI_2$ for surface passivation and LiF as an anti-reflective coating (Supplementary Fig. 7 and Table 1). The $EDAI_2$ layer has a nominal thickness of less than one nanometre and consequently does not affect the bandgap or the bulk of the perovskite absorber layer (Supplementary Fig. 7). With a bandgap of 1.64 eV, as extracted from corresponding EQE measurements (Fig. 2d), this performance represents the highest reported PCE for fully vacuum-processed WBG (E_g > 1.6 eV) PSCs in the p–i–n architecture using a pure MA-based composition[39]. We note that the bandgap derived from the first-order derivative of the EQE (~1.644 eV) is slightly lower than the PL-derived bandgap (~1.652 eV). Such small offsets are expected due to the different physical processes probed by each technique, with the EQE inflection-point method generally considered the most reliable estimate of the photovoltaic bandgap as discussed by Kirchartz and co-workers[44]. SEM imaging reveals large grains with a compact structure throughout the absorber layer (Fig. 1b). The additional annealing step further improves film morphology without altering its composition or crystallinity (Supplementary Figs. 8 and 9). Light-intensity-dependent *J*–*V* measurements of the passivated devices reveal an ideality factor of n_{id} = 1.50 (Fig. 1e and Supplementary Table 3). This value is consistent with relatively low bulk recombination losses, while also indicating moderate interfacial or trap-assisted recombination contributions. Such recombination contributions point to interface-related limitations that are not yet fully suppressed. Reducing these recombination losses is a key objective for future device optimization and improved interfacial passivation.

The long-term stability under 1-sun illumination and thermal stress (ISOS-L2) was evaluated at 65 °C and 85 °C (Supplementary Fig. 10). At both temperatures, the devices retain more than 95% of their initial performance throughout the entire testing period exceeding 400 hours. Notably, degradation is sufficiently slow that T95, the time required for the performance to decline to 95% of its initial value, is not reached in any of the two cases, with linear extrapolation suggesting values exceeding 500 hours. Altogether, these results establish CSS as an effective process for the fabrication of WBG PSCs with good stability, as was also recently demonstrated for a $MAPbI_3$ perovskite composition[33].

Furthermore, to study the suitability of our CSS-processed WBG PSCs for tandem applications, semitransparent (ST) devices were fabricated. PCEs of the ST PSCs reach more than 16% under top illumination (Table 1 and Supplementary Figs. 11 and 12), showing great potential for the integration of CSS-processed perovskite absorbers into tandem architectures. In addition, replacing BCP by ALD-deposited SnO_2 proves effective in mitigating damage on the stack induced by the deposition of the top transparent electrode leading to more reproducible ST device performances (Supplementary Fig. 13).

Monolithic 2-terminal perovskite/silicon tandem solar cells

The CSS-processed WBG perovskite absorbers were successfully integrated into monolithic perovskite/silicon TSCs. To evaluate the versatility of the developed CSS process, silicon heterojunction bottom cells featuring three different morphologies were selected, namely planar, sub-micrometre pyramidal (nano-textured) and micrometre-scale pyramidal (micro-textured), representing both research-scale and industrially relevant architectures. The layer stack of the fabricated 2T TSCs (Si/ITO/NiO_x/p-doped TaTm/TaTm/$MAPb(I_{0.79}Br_{0.21})_3$/$EDAI_2$/$C_{60}$/$SnO_x$/IZO/Ag) was the same for all three configurations (Fig. 3a and Supplementary Fig. 14). Notably, the perovskite deposition parameters were kept identical across all three bottom-cell morphologies, while only the thicknesses of the charge transport layers and electrodes were adjusted to account for the increased surface area on the textured substrates.

All configurations exhibit comparable performance, indicating a robust and solid process tolerance of CSS regardless of the

https://doi.org/10.1038/s41560-026-02068-9

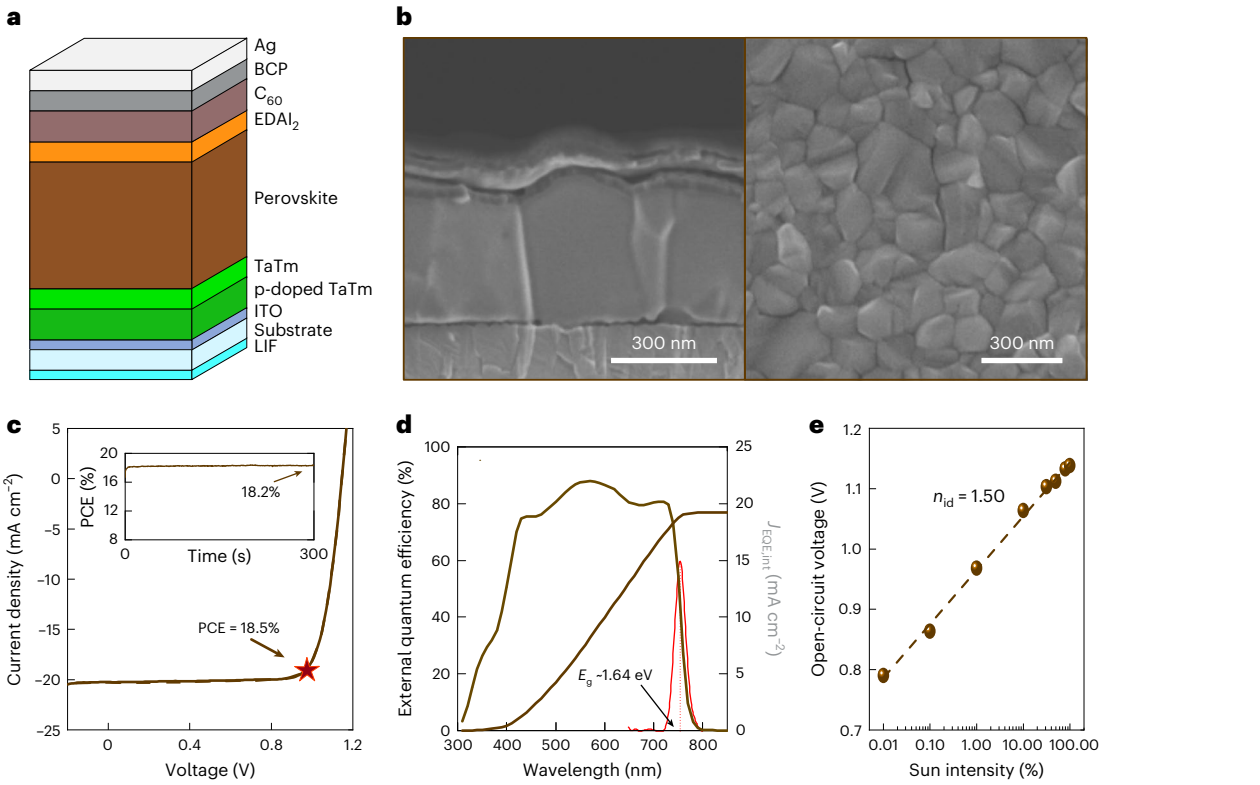

Fig. 2 | Single junction p–i–n wide-bandgap perovskite solar cell via close-space sublimation. a, Fully vacuum-processed layer stack of fabricated perovskite solar cells (PSCs) in p–i–n architecture with $EDAI_2$ and LiF as surface passivation and anti-reflective coating, respectively. **b**, SEM images of cross-section of PSC (left) and corresponding surface of perovskite absorber layer (right). **c**, Current–voltage (*J*–*V*) characteristic of champion PSC with maximum power point tracking for 300 seconds. **d**, Corresponding external quantum efficiency (EQE) measurement with integrated current density and highlighted bandgap as derived by the derivative of the EQE. **e**, Light-intensity-dependent V_{OC} measurements, taken from corresponding *J*–*V* measurements, with extracted ideality factor (n_{id}).

substrate surface morphology (Fig. 3b). *J*–*V* measurements of the best-performing devices in each configuration reveal comparable V_{OC} ranging from 1.77–1.81 V and fill factor (FF) around 75%. The planar device achieves the highest V_{OC} (1.81 V), suggesting reduced interfacial recombination. In contrast, the nano- and micro-textured devices exhibit higher J_{SC}s of 18.1 mA cm^{-2} and 18.3 mA cm^{-2}, respectively, attributed to enhanced light trapping and increased optical path length enabled by surface texturing. Among all configurations, the micro-textured device achieves the highest PCE of 24.3%, outperforming the planar (23.5%) and nano-textured (23.7%) configurations. This performance is among the highest reported PCEs for fully textured 2T perovskite/silicon TSCs employing a device stack with all individual layers deposited exclusively via vacuum-based deposition processes[13,45]. Preliminary outdoor stability data obtained from a single tandem device indicate stable operation under real-world conditions (Supplementary Fig. 15). These results highlight the robustness of the CSS process across different bottom-cell morphologies and underscore its potential as a scalable, solvent-free deposition technique for high-throughput fabrication of efficient 2T TSCs on industrially relevant silicon substrates.

EQE analyses reveal a consistent integrated photocurrent density for the perovskite top cells across all three bottom-cell morphologies, ranging from 18.0 mA cm^{-2} to 18.7 mA cm^{-2} (Fig. 3c), indicating uniform optical and electronic quality of the top absorber. The remaining variations in EQE of the perovskite top cell are governed by the interplay between substrate texture and the effective perovskite absorber thickness in the short wavelength range (400–500 nm), and by the thickness dependence in the longer-wavelength range (500–700 nm) (Supplementary Fig. 16). Cross-sectional SEM images (Fig. 4a) show that the micro-textured device forms a thinner effective perovskite layer, reducing the optical path and lowering top-cell absorption, consistent with the increased silicon bottom-cell response. As anticipated, the integrated photocurrent density of the silicon bottom cell exhibits a clear dependence on surface texturing, increasing from 16.4 mA cm^{-2} for the planar configuration to 18.0 mA cm^{-2} for nano-textured and 19.3 mA cm^{-2} for micro-textured surfaces. These findings are in excellent agreement with the trends observed in the *J*–*V* characteristics presented in Fig. 3b. Irrespective of the texture, all perovskite top cells exhibit identical bandgaps of ~1.66 eV as extracted from EQE, further demonstrating the robustness of the perovskite formation by our CSS process (Supplementary Fig. 17). We note that the observed bandgap differences between SJ and tandem devices stem from variations in the processing, that is, the inorganic scaffold preparation, which itself changes moderately depending on the underlying substrate as reported in literature[46]. Compositional engineering of the perovskite absorber layer presents a promising strategy to optimize current matching tailored to the specific optical and electronic characteristics of each silicon bottom-cell morphology.

Suns-V_{OC} with selective illumination measurements reveal a consistent voltage generation of ~1.09 V for each perovskite top cell across all configurations, further underscoring the robustness of CSS (Fig. 3d). These measurements were conducted by selectively exciting the perovskite or silicon sub-cell using collimated LEDs at 450 nm and 940 nm, respectively. In combination with EQE analyses, the illumination intensities corresponding to one sun at the selected wavelengths (450 nm for the perovskite top cell and 940 nm for the silicon bottom cell) can be accurately determined, allowing for the extraction of the V_{OC} of each sub-cell (Supplementary Fig. 18). Parasitic absorption and

https://doi.org/10.1038/s41560-026-02068-9

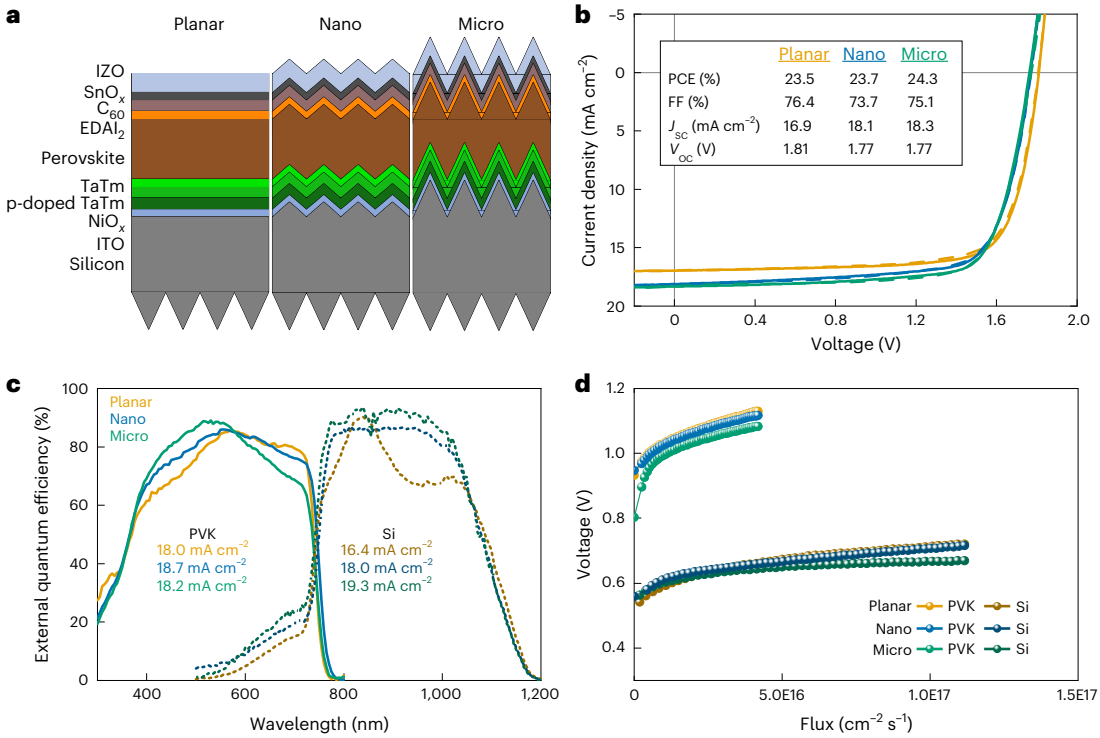

Fig. 3 | Integration of the close-space-deposited wide-bandgap perovskite into monolithic perovskite/silicon tandem solar cells using differently textured silicon bottom cells. a, Layer stacks of fabricated two-terminal perovskite/silicon tandem solar cells (TSCs) with differently textured silicon bottom cells (planar, nano-textured and micro-textured). **b**, Current–voltage (J–V) characteristics of champion TSCs for all three configurations with corresponding photovoltaic parameters. **c**, External quantum efficiency (EQE) analysis of champion TSCs on planar, nano-textured and micro-textured silicon bottom cells. **d**, Suns-V_{OC} with selective illumination measurements of both sub-cells of corresponding TSCs.

PL from blue excitation can generate a contribution from the silicon bottom cell to the voltage vs flux measurement of the perovskite top cell, which can lead to an overestimation of the perovskite V_{OC}. To mitigate this, the V_{OC} of the perovskite top cell is estimated by subtracting the V_{OC} of the silicon bottom cell (Supplementary Fig. 18) from the measured tandem device V_{OC} (Fig. 3b). Moreover, all three perovskite top cells exhibit a clear logarithmic dependence of voltage on light flux, indicating a low-shunt leakage and efficient carrier extraction[45]. The observed uniformity in V_{OC}, together with the identical bandgaps of ~1.66 eV, further reinforces the reproducibility and reliability of the CSS process.

In-depth sub-cell characterization, combining EQE and Suns-V_{OC} analyses, demonstrates the capability of CSS to produce high-quality perovskite films on both planar and textured silicon substrates. Notably, these properties remain unchanged over a 5-minute process window, irrespective of the underlying substrate morphology, providing a practical margin for processing variations and confirming a wide and reliable process window essential for scalable, industrial tandem device fabrication (Supplementary Fig. 19).

Cross-sectional SEM imaging confirms a similar perovskite layer morphology across all three silicon bottom-cell morphologies despite their different surface topographies (Fig. 4a). All configurations exhibit conformal coverage with similar horizontal grain sizes and pronounced columnar growth, comparable to the SJ reference. Furthermore, complete coverage of all bottom-cell morphologies by the perovskite absorber is observed, demonstrating the excellent deposition uniformity enabled by CSS (Supplementary Fig. 21). For the micro-textured Si-based tandems, cross-section SEM images with different magnifications clearly show a conformal deposition as shown in Supplementary Fig. 22. Thickness measurements along the optical axis (light incident direction) reveal comparable perovskite film thicknesses of 460–480 nm across all configurations. However, when measured perpendicular to the pyramid facets, the effective perovskite film thickness on nano- and micro-textured substrates is reduced to approximately 300 nm due to the increased surface area, as expected. It is highlighted that unlike solution-based hybrid process routes that commonly lead to complete filling of nano-textured silicon features[47–50], our CSS process yields a truly conformal perovskite layer that follows the nano-texture without penetrating into it. This very substantial difference in coverage bears the potential of a conceptual advantage when it comes to optimization of light management and light incoupling at the front interface of perovskite/Si tandem solar cells using nano-textured Si bottom cells. GIWAXS analyses (Fig. 4b) show similar patterns for all three configurations with no preferred growth orientation of the perovskite crystallites, as confirmed by the corresponding pole figures (Supplementary Figs. 23 and 24). Additionally, all films exhibit similar degrees of crystallinity, with comparable full-width at half-maximum values for the (100)-perovskite peak, indicating a consistent microstructure across all silicon bottom-cell morphologies. Spatially resolved k-imaging derived from intensity-dependent PL-mapping reveals comparable perovskite layer qualities and great homogeneity across the entire active area (1 cm^2) of the substrate in all three cases (Fig. 4c)[51,52]. For both textured configurations (nano- and micro-textured) the perovskite layers exhibit similar k-factor values of ~1.2–1.3, while the perovskite layer in the planar configuration shows slightly higher k-factors of ~1.3–1.4. These results further highlight the robustness of the CSS process, which enables uniform, conformal and high-quality perovskite film formation with consistent morphological, microstructural and optoelectronic properties independent of the texture of the underlying substrate and without the need to adjust deposition parameters. Notably, this robustness also extends to the underlying surface chemistry, with chemically distinct hole-transporting layers (HTLs) yielding virtually identical optoelectronic and structural properties (Supplementary Fig. 25).

https://doi.org/10.1038/s41560-026-02068-9

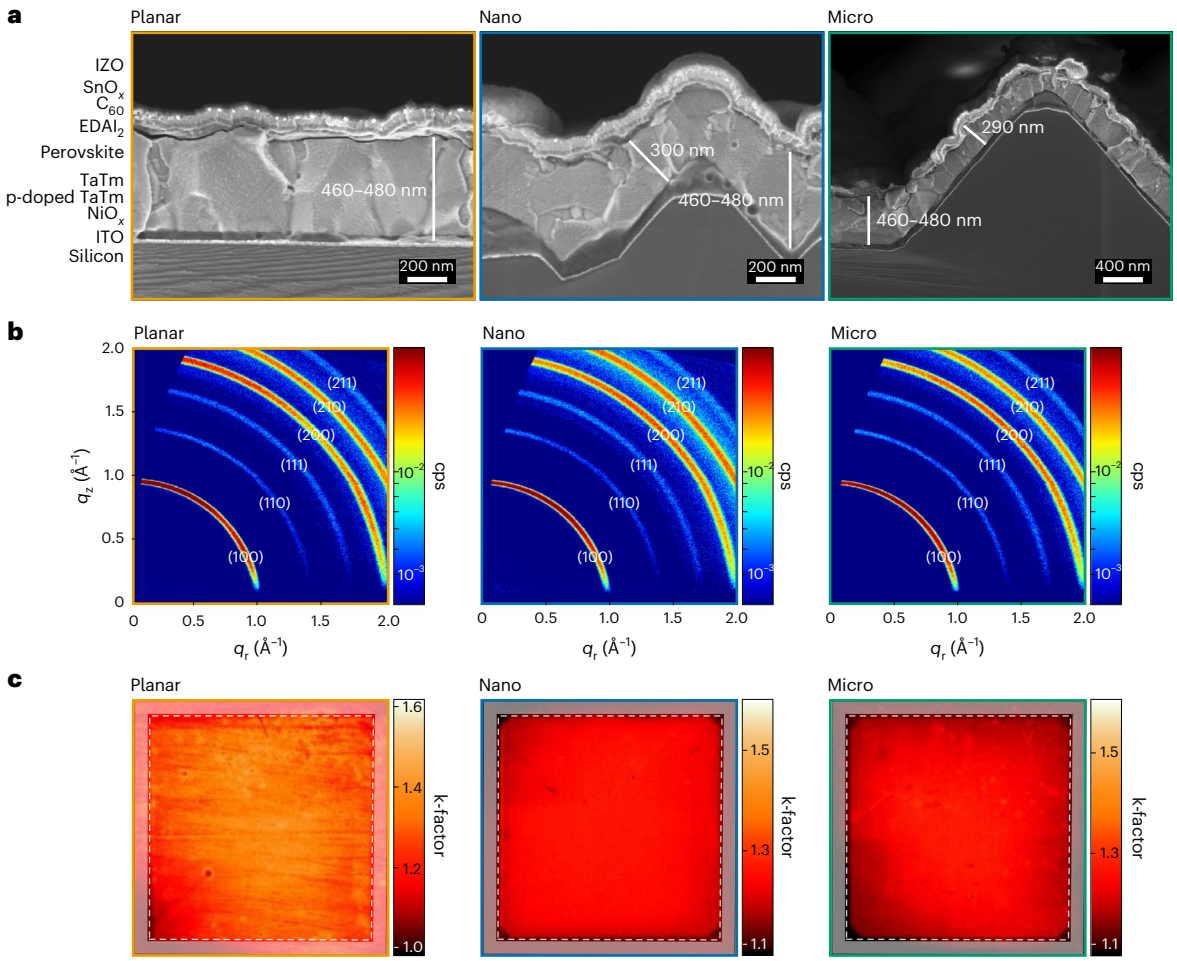

Fig. 4 | Morphological and structural analysis of perovskite films deposited on silicon bottom cells featuring different surface morphologies. a, Cross-sectional scanning electron microscopy (SEM) images of finished tandem solar cells (TSCs) on planar, nano- and micro-textured silicon bottom cells. **b**, Grazing-incident wide-angle X-ray scattering (GIWAXS) measurements of corresponding TSCs. **c**, Spatially resolved k-factor images derived from intensity-dependent photoluminescence (PL)-mapping of the active area (1 cm^2) of the perovskite thin films on planar, nano- and micro-textured silicon bottom cells. The respective histogram is shown in Supplementary Fig. 20.

This distinguishes CSS from other deposition techniques such as co-sublimation, solution-based or hybrid deposition methods, which typically require considerable process modifications to accommodate varying surface morphologies[14,53,54].

Our work pioneers CSS as a promising, industrially relevant deposition method for scalable, vacuum-based fabrication of efficient perovskite-based photovoltaics. We report the first demonstration of CSS for fully vacuum-processed WBG SJ PSCs in the p–i–n architecture, with PCEs up to 18.5% for a pure MA-based perovskite composition. These results underscore the potential of CSS to deliver competitive device performances for vapour-phase-deposited PSCs. The fast optimization cycles enabled by the rapid CSS process, compared with other typically much slower vapour-based deposition methods, will further accelerate the technological development of this technique. Notably, whereas FA-based perovskites are often considered more thermally stable, our results demonstrate that CSS-processed MA-based perovskites can also exhibit excellent stability[37]. With exceptionally short deposition times of 10 minutes, champion PCEs of 24.3% were achieved for fully vacuum-processed 2T perovskite/silicon TSCs on industrially relevant silicon bottom cells. The effective deposition rate in our work (film thickness per process time) is approximately 47 nm min^{-1}, which is around one order of magnitude higher compared to conventional thermal co- or sequential deposition from point sources[1,55]. These rates can be further increased by slightly increasing the source temperature or further reducing the source-to-substrate distance[33,56]. Importantly, CSS does not require operating the organic source at excessively high temperatures, thereby strongly suppressing temperature-induced precursor dissociation, which has been identified as the primary bottleneck for high-throughput vapour-phase deposition[19]. Whereas deposition rate is an important parameter for assessing process throughput, industrial manufacturing lines typically consist of multiple dedicated process modules operating under optimized conditions for each deposition step. Here the inorganic scaffold could be deposited using linear sublimation sources, while the organic conversion step would be realized in a separate CSS module. Production throughput could then be increased not only by increasing the deposition rates but also through the use of multiple modules along the production line[1,19,57]. Finally, the sublimation source in our CSS set-up can be readily scaled, either by increasing the geometric width of the source or by implementing shower-head-type evaporators, ultimately enabling the dynamic deposition rates required for GW-scale manufacturing. Altogether, our work establishes CSS as an innovative deposition method with great potential for cost-effective and high-throughput processing.

Conclusions

Enhancing the deposition rate of vacuum-based processes remains a key challenge for the scalable fabrication of perovskite photovoltaics.

In this work, we demonstrate a fully vacuum-based, solvent-free CSS process for the rapid deposition of MA-based WBG PSCs. We provide mechanistic insights into CSS for WBG perovskite thin-film fabrication and reveal a strategy to control the bandgap of the resulting perovskite absorber. While tuning the iodine-to-bromine ratio via the inorganic scaffold is ineffective as bromine incorporation is largely suppressed during conversion with a pure MAI organic source, this limitation can be overcome by adapting the ratio of MAI:MABr in the organic source of the CSS step. A mixed organic MAI:MABr source with a relative mass ratio of 3:1 is used to convert a sublimed PbI_2 inorganic scaffold into $MAPb(I_{0.79}Br_{0.21})_3$ with a bandgap of 1.64 eV. With an optimized layer stack, PCEs of up to 18.5% (stabilized at 18.2%) are achieved for opaque p–i–n single-junction devices. We further demonstrate the successful integration of the developed WBG perovskite absorber into 2T perovskite/silicon TSCs on silicon bottom cells with different surface morphologies (planar, nanometre-size and micrometre-size pyramids). Without adjusting the CSS deposition parameters to the different textured surfaces, the perovskite films show comparable optoelectronic properties, revealing a wide and robust process window. Furthermore, scanning electron microscopy and grazing-incidence wide-angle X-ray scattering analyses reveal similar morphologies and crystal growth of the perovskite layers on all three bottom-cell morphologies. Sub-cell characterization via external quantum efficiency and Suns-V_{OC} with selective illumination measurements reveal consistent current generation and voltage output from the perovskite top cells, regardless of the underlying silicon bottom-cell morphology. A champion PCE of 24.3% was achieved for fully vacuum-processed micro-textured perovskite/silicon TSCs. Our results highlight the versatility, scalability and industrial relevance of CSS as a high-throughput, solvent-free deposition method for efficient two-terminal perovskite/silicon TSCs.

Methods

Materials

Pre-patterned ITO-coated glass substrates were purchased from Kintec Company. TaTm (*N*4,*N*4,*N*4″,*N*4″-tetra([1,1′-biphenyl]-4-yl)-[1,1′:4′,1″-terphenyl]-4,4″-diamine) was obtained from Tokyo Chemical Industry. CS90112 (2,2′,2″-(cyclopropane-1,2,3-triylidene)tris(2-(p-cyanotetrafluorophenyl)acetonitrile)), PbI_2 (lead iodide), $PbBr_2$ (lead bromide), MAI (methylammonium iodide) and BCP (bathocuproine) were purchased from Luminescence Technology Corp. MABr (methylammonium bromide) was purchased from Greatcell Solar Materials. C_{60} (fullerene-C_{60}) was purchased from MBraun (Creaphys). $EDAI_2$ (ethylenediammonium di-iodide) was purchased from Sigma-Aldrich Co.

Film and device fabrication

Single-junction solar cells were prepared on ITO-coated glass substrates, which were subsequently cleaned with soap (2% Mucasol in water), water and isopropanol in an ultrasonic bath, followed by 20 min UV–ozone treatment. The substrates were transferred to a vacuum chamber integrated in a nitrogen-filled glovebox and evacuated to a pressure of 10^{-6} mbar for the charge extraction layers' deposition. In general, the deposition rate for the TaTm and C_{60} was 0.5 $Å s^{-1}$ while the thinner BCP was deposited at 0.2 $Å s^{-1}$. For the p-doped HTL layer TaTm and CS90112 (as p-dopant) were co-sublimed at a rate of 0.8 and 0.12 $Å s^{-1}$ by heating them at temperatures of around 300 °C and 130 °C, respectively. Ag was evaporated in a separate vacuum chamber using aluminium boats as sources. For the different inorganic precursor compositions (PbI_2, $Pb(I_{0.67}Br_{0.33})_2$, $Pb(I_{0.33}Br_{0.67})_2$, $PbBr_2$), PbI_2 and $PbBr_2$ were mixed in the desired molar ratios and melted at 360 °C in N_2 at atmospheric pressures prior to sublimation.

All inorganic scaffolds were deposited at a rate of 1 $Å s^{-1}$ attained at a temperature of 250 °C. The rate and final thickness of 250 nm were controlled in an individual quartz crystal microbalance (QCM) placed above the sublimation source. The different organic source compositions for the CSS deposition step were obtained by mixing MAI and MABr in the corresponding relative mass ratios (1 mg_{MAI}: 0 mg_{MABr}, 3 mg_{MAI}: 1 mg_{MABr}, 1 mg_{MAI}: 1 mg_{MABr}, 0 mg_{MAI}: 1 mg_{MABr}.) The precursor source was prepared by mixing methylammonium iodide (MAI) and methylammonium bromide (MABr) in the desired relative weight ratio. The materials were finely ground using a mortar and pestle until a homogeneous powder was achieved. This procedure ensured thorough blending of the components and produced a visually uniform powder mixture without observable agglomerates. This resulting fine powder was then transferred to the custom-designed powder bed (cuvette), fabricated from the same material and possessing the same dimensions as the recess in the CSS bottom plate to ensure alignment. The powder was distributed and levelled using a smooth-edged tool to create a planar, uniform surface with the cuvette edges. For every newly prepared source, a two-stage thermal tempering protocol was performed (top/bottom heaters set at 100 °C): first, 1 hour at atmospheric pressure, followed by 1 hour at 1 mbar.

Before experimental use (to establish source reliability) each new source batch is validated through a standard optimization protocol in which initial test conversions are performed and characterized (XRD, PL and absorbance measurements). In some cases, full devices are completed to verify that performance parameters remain consistent with previous benchmarks. Once the stability of the new source is confirmed, it is then used for regular experimental rounds.

Furthermore, to guarantee consistency between the first and subsequent conversion runs, a pre-deposition conditioning procedure was implemented before each experimental round. This consisted of two stabilization cycles where the source and substrate plates were heated to the target processing temperature under a vacuum of 1 mbar in the absence of precursor substrates. This ensures that the initial deposition occurs only after the source surface has reached a stable evaporation equilibrium.

The samples were placed above the source with a gap of 3 mm before heating the source to 100 °C. The chamber was then pumped down to 1 mbar and kept at this pressure during deposition. After that, the chamber is vented with N_2 and brought back to atmospheric pressure. The additional annealing step (10 minutes at 100 °C) is carried out in a humidity-controlled set-up with a relative humidity of ~35%. Samples prepared for material characterization were, in some cases, dynamically washed with 100 µl isopropanol for 20 s at 3,000 rpm. In contrast, all samples processed into solar cells were fabricated without any washing step. A direct comparison of device performance for cells prepared with and without washing confirms that this step has no measurable impact on photovoltaic performance (Supplementary Fig. 26). $EDAI_2$ surface passivation layer was deposited in a high vacuum chamber at 10^{-6} mbar at a rate of about 0.1–0.15 $Å s^{-1}$.

For tandem solar cell fabrication, silicon bottom cells were cleaned by sonicating for 5 min in acetone, then 5 minutes in IPA followed by a 15 min UV–ozone treatment. The additional NiO_x HTL layer (15 nm for planar and 25 nm for textured silicon bottom cells) was sputtered from a NiO_x target using 100 W power with pure Ar at 1 mTorr on the silicon bottom cell with ITO layer. All other charge transport extraction layers, namely p-doped TaTm-CS90112, intrinsic TaTm and C_{60} were deposited using the same protocol as for the single-junction devices. However, to account for the increased surface area of the textured devices (nano- and micro-textured) the deposited thickness was increased by a factor of 1.7. This adjustment was not applied in the case of the planar tandem solar cell. For the tandem devices BCP is replaced by ALD-deposited SnO_2, which serves as buffer layer to protect the underlaying stack from the harsher TCO deposition. SnO_2 is deposited via ALD using an Arradiance's GEMStar XT Thermal ALD system integrated into an N_2-filled glovebox. For SnO_2 deposition, the ALD chamber is heated to 60 °C, the bottle containing the Sn precursor tetrakis(dimethylamino) tin (TDMASn) was heated to 60 °C and the bottle of water (oxidizer) was not heated. The precursor manifolds were heated to 115 and 140 °C, respectively. The SnO_2 deposition process consists of a series of purges

of TDMASn for 550 ms and water vapour for 200 ms, each of them followed by N_2 purges to clear off the precursors from the ALD chamber. For the front contact, a 45 nm IZO layer was used as a transparent electrode, deposited via sputtering. The active area of 1.04 cm^2 was defined by the subsequently vacuum-deposited Ag electrode (350 nm and 600 nm for planar and textured configurations, respectively, with three additional 100-µm-thick grid fingers).

The silicon heterojunction bottom cells were fabricated using industry-standard n-type Czochralski Si wafers. The planar silicon bottom cells were prepared as described in ref. 58. The nano-textured silicon bottom cells were prepared similarly to the micro-textured bottom cells in ref. 59, using an adapted surfactant during KOH texturing to obtain submicron-sized pyramids. The micro-textured silicon bottom cells were prepared as described in ref. 60. The rear contact is comprised of ITO/Ag and the front recombination junction was prepared by sputtering a thin layer of ITO through a shadow mask.

Solar cell characterization

J–V curves of single-junction devices were recorded using a Keithley 2612 A source meter in a −0.2 and 1.2 V voltage range, with 0.01 V steps and integrating the signal for 20 ms after a 10 ms delay, corresponding to a scan speed of about 0.33 V s^{-1}. The devices were illuminated under a Wavelabs Sinus 70 LED solar simulator. The light intensity was adjusted before every measurement using a calibrated Si reference diode. The active area, defined as the overlap between the bottom ITO and the top metal electrodes, was 5.5 × 1.5 mm^2. For the characterization under illumination, a shadow mask defining an area of 5 × 1 mm^2 was used.

The *J–V* characteristics of the perovskite/silicon tandem solar cells were measured with a class AAA LED-based solar simulator (Wavelabs, LS-2) with a scan rate set at 0.6 V s^{-1} using a source meter (Keithley 2400) with an air-mass 1.5 global (AM1.5 G) spectra (100 mW cm^{-2}). The solar simulator irradiation intensity was calibrated using a certified silicon solar cell (Fraunhofer ISE). The measurement was performed in ambient atmosphere. A shadow mask defining an area of 1 × 1 cm^2 was used was the measurements.

For the sensitive external quantum efficiency (EQE) measurements of single-junction devices, the cell was illuminated by a QuartzTungsten-Halogen lamp (Newport Apex 2-QTH) through a monochromator (Newport CS130-USB-3-MC), a chopper at 279 Hz and a focusing lens. The device current was measure as a function of energy from 2.1 eV to 1.2 eV in 0.02 eV steps using a lock-in amplifier. The system was calibrated, and the solar spectrum mismatch was corrected using a calibrated silicon reference cell. Fast EQE measurements were performed on a QE-R system from Enlitech.

In the case of monolithic perovskite/silicon tandem solar cells, EQE was measured using an Enlitech QE-R Quantum Efficiency System, following a procedure previously reported in ref. 45. The spectral response of each sub-cell was measured in the 300 to 1,200 nm range using beam spot of approximately 1 mm^2. During the measurement, a halogen lamp is employed to provide light bias to the non-measured sub-cell. To isolate the perovskite top cell, an 850-nm long-pass filter was applied to the halogen lamp to saturate the current in the silicon heterojunction (SHJ) bottom cell, whereas a 550 nm short pass filter was used when probing the SHJ bottom cell to saturate the perovskite top cell. Under these biasing conditions, a current mismatch is generated, which introduces a shift in the operating voltage of the sub-cell under measurement, forcing it into reverse bias. Consequently, an external voltage bias is needed restore short-circuit conditions, corresponding approximately to the V_{OC} of the non-measured sub-cell: ~0.6 V for the top cell and ~1.0 V for the SHJ bottom cell.

Suns-V_{OC} with selective illumination enables the estimation of the open-circuit voltage (V_{OC}) generated by each sub-cell in a tandem device. The measurement is performed by illuminating each sub-cell independently and measuring the resulting V_{OC}. Specifically, a blue LED with a peak wavelength of 450 nm is used to excite the perovskite sub-cell, whereas a 940 nm diode selectively illuminates the silicon sub-cell.

The photoluminescence spectra were measured with an Avantes Avaspec2048 spectrometer and films were illuminated with a diode laser of Integrated Optics, emitting at 515 nm. All the spectra were collected with an integration time of 1 s.

X-ray diffraction (XRD) patterns were collected in Bragg–Brentano geometry on an Empyrean PANalytical powder diffractometer with a copper anode operated at 45 kV and 40 mA and Rigaku Mini Flex–600 C operated at 40 kV and 15 mA with a copper anode.

Scanning Electron Microscopy (SEM) was performed with a high-resolution field-emission Hitachi SU8010 microscope operating at an accelerating voltage of 2 kV over platinum-metallized samples. Steady-state photocarrier grating measurements were carried out using a He–Ne laser with 15 mW power and 632 nm wavelength.

The grazing-incidence wide-angle X-ray scattering (GIWAXS) images were acquired with a Bruker D8 Advance machine. Primary track: unpolarized Cu K-alpha X-ray source (40 kV, 40 mA), Goebel mirror, 0.5 mm micromask, 0.3 mm snout; secondary track: DECTRIS Eiger2 R 500 2D detector; sample-to-detector distance: 118.1 mm. A grazing-incidence angle of 1.7° and an exposure time of 1 h were employed for measurement. GIWAXS images processing and analysis were performed utilizing the GIXSGUI MATLAB toolboxes[61].

Grazing-incidence X-ray diffraction (GIXRD) measurements were performed using a PANalytical Empyrean diffractometer equipped with a Cu K-alpha X-ray source operated at 45 kV and 40 mA. The incident beam was shaped by a W/Si parabolic multilayer (Goebel) mirror followed by a hybrid monochromator 2xGe(220) and fixed 1/32° divergence slit.

Measurements were carried out in reflection geometry with a fixed incident angle in range of ω = 0.3 to 2°. Diffraction patterns were acquired by scanning the detector in the 2θ range from 11° to 16° with a step size of 0.05° in continuous mode with integration time of 2.64 s per step. Diffracted intensities were collected using a PIXcel1D detector equipped with 0.02 rad Soller slits and 0.1 mm parallel-plate collimator.

For k-Imaging (intensity-dependent photoluminescence-mapping), two 467 nm LED bars powered excite the sample in an 45° symmetrical alignment. The image is recorded by a sCMOS camera equipped with a macro zoom lens and an exposure time of 500 ms. To eliminate the detection of excitation light and other noise, a 695 nm absorptive long-pass filter is attached to the lens and a background correction performed. Images are recorded intensity dependent within an excitation range, equivalent to 0.005–0.2 suns based on photon flux. The k-factor is extracted as the exponent from fitting the intensity-dependent PL intensities pixel-wise with a power law model and aggregated as a heat map[52].

Reporting summary

Further information on research design is available in the Nature Portfolio Reporting Summary linked to this article.

Data availability

The data that support the findings of this study are available within the Article and its Supplementary Information. The data generated during and/or analysed during the current study are available via the KITopen repository under a CC-BY 4.0 Creative Commons Attribution license at https://doi.org/10.35097/nfpuwnntws6pu3yx (ref. 62).

References

1. Abzieher, T. et al. Vapor phase deposition of perovskite photovoltaics: short track to commercialization?. *Energy Environ. Sci.* **17**, 1645–1663 (2024).
2. Kosasih, F. U., Erdenebileg, E., Mathews, N., Mhaisalkar, S. G. & Bruno, A. Thermal evaporation and hybrid deposition of perovskite solar cells and mini-modules. *Joule* **6**, 2692–2734 (2022).

3. Vaynzof, Y. The future of perovskite photovoltaics—thermal evaporation or solution processing?. *Adv. Energy Mater.* **10**, 2003073 (2020).
4. Aydin, E. et al. Pathways toward commercial perovskite/silicon tandem photovoltaics. *Science* **383**, 1–13 (2024).
5. Yang, C. et al. Achievements, challenges, and future prospects for industrialization of perovskite solar cells. *Light Sci. Appl.* **13**, 227 (2024).
6. Jacobsson, T. J. et al. An open-access database and analysis tool for perovskite solar cells based on the FAIR data principles. *Nat. Energy* **7**, 107–115 (2022).
7. Abzieher, T. et al. Continuous flash sublimation of inorganic halide perovskites: overcoming rate and continuity limitations of vapor deposition. *J. Mater. Chem. A* **12**, 8405–8419 (2024).
8. National Laboratory of the Rockies. Best research-cell efficiency chart. *NLR* https://www.nlr.gov/pv/cell-efficiency (2026).
9. Ritzer, D. B. et al. Upscaling of perovskite solar modules: the synergy of fully evaporated layer fabrication and all-laser-scribed interconnections. *Prog. Photovoltaics Res. Appl.* **30**, 360–373 (2022).
10. Paliwal, A., Zanoni, K. P. S., Roldán-Carmona, C., Hernández-Fenollosa, M. A. & Bolink, H. J. Fully vacuum-deposited perovskite solar cells in substrate configuration. *Matter* **6**, 3499–3508 (2023).
11. Ávila, J., Momblona, C., Boix, P. P., Sessolo, M. & Bolink, H. J. Vapor-deposited perovskites: the route to high-performance solar cell production?. *Joule* **1**, 431–442 (2017).
12. Feng, J. et al. High-throughput large-area vacuum deposition for high-performance formamidine-based perovskite solar cells. *Energy Environ. Sci.* **14**, 3035–3043 (2021).
13. Roß, M. et al. Co-evaporated formamidinium lead iodide based perovskites with 1000 h constant stability for fully textured monolithic perovskite/silicon tandem solar cells. *Adv. Energy Mater.* **11**, 2101460 (2021).
14. Gil-Escrig, L. et al. Fully vacuum-processed perovskite solar cells on pyramidal microtextures. *Solar RRL* **5**, 2000553 (2021).
15. Zhou, J. et al. Highly efficient and stable perovskite solar cells via a multifunctional hole transporting material. *Joule* **8**, 1691–1706 (2024).
16. Alvianto, E. et al. Industry-compatible fully laminated perovskite-CIGS tandem solar cells with co-evaporated perovskite. *Adv. Mater.* **37**, 2505571 (2025).
17. Piot, M. et al. Fast coevaporation of 1 µm thick perovskite solar cells. *ACS Energy Lett.* **8**, 4711–4713 (2023).
18. Dewi, H. A., Erdenebileg, E., De Luca, D., Mhaisalkar, S. G. & Bruno, A. Accelerated $MAPbI_3$ co-evaporation: productivity gains without compromising performance. *ACS Energy Lett.* **9**, 4319–4322 (2024).
19. Petry, J. et al. Industrialization of perovskite solar cell fabrication: strategies to achieve high-throughput vapor deposition processes. *EES Solar* **1**, 404–418 (2025).
20. Ihrenberger, J. et al. Solution-free growth of cspbbr3 perovskite films using a fast and scalable close space sublimation method. *Cryst. Growth Des.* **24**, 5542–5548 (2024).
21. Rodkey, N. et al. Close-space sublimation as a scalable method for perovskite solar cells. *ACS Energy Lett.* **9**, 927–933 (2024).
22. Scarpulla, M. A. et al. CdTe-based thin film photovoltaics: recent advances, current challenges and future prospects. *Solar Energy Mater. Solar Cells* **255**, 112289 (2023).
23. Li, G., Ho, J. Y. L., Wong, M. & Kwok, H. S. Low cost, high throughput and centimeter-scale fabrication of efficient hybrid perovskite solar cells by closed space vapor transport. *Physica Status Solidi RRL* **10**, 153–157 (2016).
24. Hu, S. et al. Vapor–solid reaction techniques for the growth of organic–inorganic hybrid perovskite thin films. *Small* **21**, 2410865 (2025).
25. Guesnay, Q. et al. Pizza oven processing of organohalide perovskites (POPOP): a simple, versatile and efficient vapor deposition method. *Adv. Energy Mater.* **14**, 2303423 (2024).
26. Wang, Y. et al. Grain boundary elimination via recrystallization-assisted vapor deposition for efficient and stable perovskite solar cells and modules. *Adv. Mater.* **35**, 2304625 (2023).
27. Duan, C. et al. Oriented growth for efficient and scalable perovskite solar cells by vapor–solid reaction. *Adv. Funct. Mater.* **34**, 2313435 (2024).
28. Duan, C. et al. Stoichiometric gradient rebalancing achieves surface reconstruction and bulk homogenization in high-performance vapor-deposited perovskite solar cells. *J. Mater. Chem. A* **13**, 24675–24684 (2025).
29. Dou, Y. et al. Enhanced buried interface engineering for efficient inverted perovskite solar cells fabricated via vapor–solid reaction. *Small Methods* **9**, 2401339 (2025).
30. Kuba, A. G. et al. Bandgap tunable two-step vapor-deposited perovskite absorbers for perovskite-silicon tandem solar cells. *ACS Energy Lett* https://doi.org/10.1021/acsenergylett.6c00156 (2026).
31. Zhang, Y. et al. Low pressure chemical vapor deposited perovskite enables all vacuum-processed monolithic perovskite-silicon tandem solar cells. *Adv. Energy Mater.* **15**, 2405377 (2025).
32. Xiong, W. et al. Achieving high-quality wide bandgap perovskite thin films via regulating the halide ion exchange order in vapor-solid reaction. *Solar RRL* **9**, e2500053 (2025).
33. Gomar-Fernández, I. et al. Large-area close-space sublimation enables the fabrication of efficient and stable perovskite solar cells. *EES Solar* **1**, 1126–1134 (2025).
34. Mahboubi Soufiani, A. et al. Sequentially evaporated wide bandgap perovskite absorber for large-area and reproducible fabrication of solar cells. *Solar RRL* **9**, e2500412 (2025).
35. Yan, J. et al. Crystallization process for high-quality $Cs_{0.15}$ $FA_{0.85}$ $PbI_{2.85}$ $Br_{0.15}$ film deposited via simplified sequential vacuum evaporation. *ACS Appl. Energy Mater.* **6**, 10265–10273 (2023).
36. Dewi, H. A. et al. Efficient bandgap widening in co-evaporated $MAPbI_3$ perovskite. *Sustain. Energy Fuels* **6**, 2428–2438 (2022).
37. Li, H. et al. Sequential vacuum-evaporated perovskite solar cells with more than 24% efficiency. *Sci. Adv.* **8**, eabo7422 (2022).
38. Igual-Muñoz, A. M. et al. Room-temperature vacuum deposition of $CsPbI_2Br$ perovskite films from multiple sources and mixed halide precursors. *Chem. Mater.* **32**, 8641–8652 (2020).
39. Gil-Escrig, L. et al. Efficient and thermally stable wide bandgap perovskite solar cells by dual-source vacuum deposition. *Adv. Funct. Mater.* **33**, 2214357 (2023).
40. Li, G., Ho, J. Y.-L., Wong, M. & Kwok, H. S. Reversible anion exchange reaction in solid halide perovskites and its implication in photovoltaics. *J. Phys. Chem. C* **119**, 26883–26888 (2015).
41. Kim, G. et al. In Situ vapor-phase halide exchange of patterned perovskite thin films. *Small* **17**, 2006737 (2021).
42. Ivanov, I. L. et al. Vapor pressure of methylammonium halides. Part II: vapor pressure and standard entropy of methylammonium bromide. *Thermochim. Acta* **674**, 58–62 (2019).
43. Harding, A. J., Dobson, K. D., Ogunnaike, B. A. & Shafarman, W. N. Thermal and structural characterization of methylammonium- and formamidinium-halide salts. *Phys. Status Solidi A* **218**, 2100246 (2021).
44. Krückemeier, L., Rau, U., Stolterfoht, M. & Kirchartz, T. How to report record open-circuit voltages in lead-halide perovskite solar cells. *Adv. Energy Mater.* **10**, 1902573 (2020).
45. Chozas-Barrientos, S. et al. Molecular recombination junction for vacuum-deposited perovskite/silicon two-terminal tandem solar cells. *ACS Energy Lett* **10**, 1733–1740 (2025).

46. Diercks, A. et al. Sequential evaporation of inverted $FAPbI_3$ perovskite solar cells—impact of substrate on crystallization and film formation. *ACS Energy Lett.* **10**, 1165–1173 (2025).
47. Chen, B. et al. Blade-coated perovskites on textured silicon for 26%-efficient monolithic perovskite/silicon tandem solar cells. *Joule* **4**, 850–864 (2020).
48. Yang, G. et al. Towards efficient, scalable and stable perovskite/silicon tandem solar cells. *Nat. Photonics* **19**, 913–924 (2025).
49. Jia, L. et al. Efficient perovskite/silicon tandem with asymmetric self-assembly molecule. *Nature* **644**, 912–919 (2025).
50. Li, Y. et al. Nanoscale size control of Si pyramid texture for perovskite/Si tandem solar cells enabling solution-based perovskite top-cell fabrication and improved Si bottom-cell response. *Adv. Mater. Interfaces* **10**, 2300504 (2023).
51. Hacene, B. et al. Imaging of recombination rates and lifetime in perovskite thin film processing. *Small Methods* **9**, 2402119 (2025).
52. Petermann, J. et al. Advanced photoluminescence imaging method for robust and scalable perovskite quality monitoring in monolithic tandem solar cells. *Solar RRL* **9**, e2500074 (2025).
53. Er-raji, O. et al. Toward efficient and industrially compatible fully textured perovskite silicon tandem solar cells: controlled process parameters for reliable perovskite formation. *Prog. Photovoltaics Res. Appl.* **33**, 86–99 (2025).
54. Pappenberger, R. et al. Versatile two-step process for perovskite-based tandem photovoltaics. *Solar RRL* **9**, 2500193 (2025).
55. Feeney, T. et al. High-rate FA-based co-evaporated perovskites: understanding rate limitations and practical considerations to overcome their impact. *Adv. Funct. Mater.* **36**, e17873 (2026).
56. Zhang, G. et al. Ultrafast growth of high-quality $Cs_{0.14}$ $FA_{0.86}$ $Pb(Br_x I_{1-x})_3$ thin films achieved using super-close-space sublimation. *ACS Appl. Energy Mater.* **5**, 5797–5803 (2022).
57. Swanson, D. E. et al. Single vacuum chamber with multiple close space sublimation sources to fabricate CdTe solar cells. *J. Vac. Sci. Technol. A* **34**, 021202 (2016).
58. Taddei, M. et al. Diamine surface passivation and postannealing enhance the performance of silicon-perovskite tandem solar cells. *ACS Appl. Mater. Interfaces* **17**, 38754–38762 (2025).
59. Shen, X. et al. Crystal-facet-directed all-vacuum-deposited perovskite solar cells. *Nat. Mater.* https://doi.org/10.1038/s41563-026-02494-w (2026).
60. Pesch, R. et al. Efficient perovskite/silicon tandem solar cells using hybrid two-step inkjet printing with edge isolation precision. *Small Sci.* **5**, 2500362 (2025).
61. Jiang, Z. *GIXSGUI*: a MATLAB toolbox for grazing-incidence X-ray scattering data visualization and reduction, and indexing of buried three-dimensional periodic nanostructured films. *J. Appl. Crystallogr.* **48**, 917–926 (2015).
62. Research data for: close space sublimation as a versatile deposition process for efficient perovskite silicon tandem solar cells. *KITopen* https://doi.org/10.35097/nfpuwnntws6pu3yx (2026).

Acknowledgements

The cooperation and research exchange enabling this work was funded by the Karlsruhe House of Young Scientists (KHYS). We gratefully acknowledge financial support by the Helmholtz Association (project Zeitenwende, Solar Technology Acceleration Platform (Solar TAP), programme-oriented funding period IV of the Helmholtz Association (Materials and Technologies for the Energy Transition, Topic 1: Photovoltaics and Wind Energy, Code: 38.01.02)), the German Federal Ministry for Economic Affairs and Energy (BMWE) through the project SHAPE (03EE1123A) and the Karlsruhe School of Optics and Photonics (KSOP), co-funded by the European Union. Views and opinions expressed are however those of the author(s) only and do not necessarily reflect those of the European Union, the European Climate, Infrastructure and Environment Executive Agency (CINEA) or the European Research Council Executive Agency (ERCEA). Neither the European Union nor the granting authority can be held responsible for them. The NEXUS project has received funding from the European Union's Horizon Europe research and innovation programme under grant agreement number 101075330. This research was carried out as part of the CETPartnership project HyPer under the joint call 2023, co-funded by the European Commission (grant agreement number 101069750) and the national funding organizations listed on the CETPartnership website (BMWE funding code 03EE1222B for KIT). This work is supported by the ERC grant LAMI-PERO (number 101087673). We also acknowledge support from the State Secretariat for Telecommunications and Digital Infrastructure, from the Ministry of Economic Affairs and Digital Transformation in the framework of the European Recovery, Transformation and Resilience Plan, with funding from European Union NextGenerationEU, project number TSI-069100-2023-0012- PERTE chip, the Comunitat Valenciana (MFA/2022/022 and CISEJI/2022/43) and from the Ministry of Science and Innovation (MCIN) and the Spanish State Research Agency (AEI): PCI2024-155048-2 project funded by MICIU/AEI/10.13039/501100011033 and co-funded by the European Union; grant RYC2019-027187-I funded by MCIN/AEI/10.13039/501100011033 and by 'ESF Investing in Your Future; PID2024-159087OB-I00 funded by MICIU/AEI/10.13039/501100011033' and 'ERDF A way of making Europe'.

Author contributions

A.D. and S.C.-B. equally contributed to conceptualization, methodology, investigation, visualization and original draft preparation. L.G.-E., F.V., I.G.-F., C.R.-C., N.R., T.Z., J.P., M. Senno and V.H. assisted in investigation, device fabrication and device characterization. P.C. and D.M. fabricated the silicon bottom cells. P.F., A.D. and S.C.-B. contributed to reviewing and editing of the manuscript. L.G.-E., M. Sessolo and P.F. assisted with supervision. U.W.P. and H.J.B. equally led the supervision, funding acquisition, project administration and reviewing and editing of the manuscript.

Funding

Open access funding provided by Karlsruher Institut für Technologie (KIT).

Competing interests

The authors declare no competing interests.

Additional information

Supplementary information The online version contains supplementary material available at https://doi.org/10.1038/s41560-026-02068-9.

Correspondence and requests for materials should be addressed to Ulrich W. Paetzold or Henk J. Bolink.

Peer review information *Nature Energy* thanks Kyungkon Kim, Jianfeng Lu, Samuel Stranks, Terry Chien-Jen Yang and the other anonymous reviewer(s) for their contribution to the peer review of this work.

nature portfolio

Corresponding author(s): Ulrich W. Paetzold, Henk J. Bolink

Solar Cells Reporting Summary

Nature Portfolio wishes to improve the reproducibility of the work that we publish. This form is intended for publication with all accepted papers reporting the characterization of photovoltaic devices and provides structure for consistency and transparency in reporting. Some list items might not apply to an individual manuscript, but all fields must be completed for clarity.

For further information on Nature Research policies, including our data availability policy see Authors & Referees.

Experimental design

Please check the following details are reported in the manuscript, and provide a brief description or explanation where applicable.

1. Dimensions

Area of the tested solar cells	☒ Yes ☐ No	Single-junction devices: 0.05 cm^2, tandem solar cells: 1 cm^2 *Explain why this information is not reported/not relevant.*
Method used to determine the device area	☒ Yes ☐ No	Shadow masks to define active area during deposition of silver electrode. *Explain why this information is not reported/not relevant.*

2. Current-voltage characterization

Current density-voltage (J-V) plots in both forward and backward direction	☒ Yes ☐ No	*State where this information can be found in the text.*
Voltage scan conditions	☒ Yes ☐ No	Single-junction devices: -0.2 and 1.2 V voltage range, with scan speed of about 0.1 Vs-1 Tandem solar cells: -0.2 and 2.0 V voltage range, with scan speed of about 0.6 Vs-1 *Explain why this information is not reported/not relevant.*
Test environment	☒ Yes ☐ No	J-V measurements were carried out in atmosphere. *Explain why this information is not reported/not relevant.*
Protocol for preconditioning of the device before its characterization	☐ Yes ☒ No	*Provide a description of the protocol.* no preconditioning of the device before characterization.
Stability of the J-V characteristic	☒ Yes ☐ No	A 300 sec. MPP-tracking of the champion single-junction solar cell was carried out. The data is shown in Figure 1 in the main manuscript. *Explain why this information is not reported/not relevant.*

3. Hysteresis or any other unusual behaviour

Description of the unusual behaviour observed during the characterization	☐ Yes ☒ No	*Provide a description of hysteresis or any other unusual behaviour observed during the characterization.* Devices show negligible hysteresis.
Related experimental data	☐ Yes ☒ No	*Provide a description of the related experimental data.* No unusual behaviour detected.

4. Efficiency

External quantum efficiency (EQE) or incident photons to current efficiency (IPCE)

☒ Yes
☐ No

Single-junction devices: Illumination by a QuartzTungsten-Halogen lamp (Newport Apex 2-QTH) through a monochromator (Newport CS130-USB-3-MC), a chopper at 279 Hz and a focusing lens. Device current was measure as a function of energy from 2.1 eV to 1.2 eV in 0.02 eV steps using a lock-in amplifier. Solar spectrum mismatch was corrected using a calibrated silicon reference cell.

Tandem solar cells: EQE was measured using an Enlitech QE-R Quantum Efficiency System. To measure the spectral response of each sub-cell in the 300 to 1200 nm range a beam spot with an area of 1 mm^2 was used. A halogen lamp was used to illuminate the sub-cell for which the EQE is not being analyzed. When the EQE of the perovskite top cell was analyzed an 850 nm long pass filter was applied to the halogen lamp to saturate the current generated by the SHJ bottom cell, and when the EQE of the SHJ bottom cell was analyzed a 550 nm short pass filter was used to saturate the current generated by the perovskite top cell.

Explain why this information is not reported/not relevant.

A comparison between the integrated response under the standard reference spectrum and the response measure under the simulator

☒ Yes
☐ No

Values from J-V analysis and EQE are shown in the main figures in the manuscript, as well as in the figures in the SI.

Explain why this information is not reported/not relevant.

For tandem solar cells, the bias illumination and bias voltage used for each subcell

☒ Yes
☐ No

Voltage bias of non-analyzed sub-cell during characterization: ~ 0.6 V for silicon bottom cells, and ~1.0 V for the perovskite top-cells

Explain why this information is not reported/not relevant.

5. Calibration

Light source and reference cell or sensor used for the characterization

☒ Yes
☐ No

Single-junction devices: Wavelabs Sinus 70 LED solar simulator and Keithley 2612A sourcemeter
Tandem solar cells: class AAA LED-based solar simulator (Wavelabs, LS-2) and Keithley 2400 sourcemeter

Solar simulator irradiation intensity was calibrated with a certified silicon solar cell in before each measurement.

Explain why this information is not reported/not relevant.

Confirmation that the reference cell was calibrated and certified

☒ Yes
☐ No

Fraunhofer ISE

Explain why this information is not reported/not relevant.

Calculation of spectral mismatch between the reference cell and the devices under test

☒ Yes
☐ No

Solar simulator intensity was calibrated to match calibration cell.

Explain why this information is not reported/not relevant.

6. Mask/aperture

Size of the mask/aperture used during testing

☒ Yes
☐ No

Shadow mask with defining area of 1 cm^2 was used for tandem solar cell measurements.

Explain why this information is not reported/not relevant.

Variation of the measured short-circuit current density with the mask/aperture area

☐ Yes
☒ No

Report the difference in the short-circuit current density values measured with the mask and aperture area.

Has not been tested.

7. Performance certification

Identity of the independent certification laboratory that confirmed the photovoltaic performance

☐ Yes
☒ No

Identify the independent certification laboratory.

Solar cells were not sent for certification.

A copy of any certificate(s)

☐ Yes
☒ No

Certificate copies should be provided in the Supplementary Information. Please state the supplementary item number.

No certification

8. Statistics

Number of solar cells tested

☒ Yes
☐ No

Min. 12 devices were tested for all single-junction configurations.

Explain why this information is not reported/not relevant.

Statistical analysis of the device performance	☒ Yes	The statistical data is represented in boxplots in the SI.
	☐ No	*Explain why this information is not reported/not relevant.*

9. Long-term stability analysis

Type of analysis, bias conditions and environmental conditions	☒ Yes	Long-term operational stability of single-junction devices was measured under combined 1-sun illumination and thermal stress (ISOS-L2): 65 °C and 85 °C (see Supplementary Fig. 5)
	☐ No	*Explain why this information is not reported/not relevant.*